AGU PUBLICATIONS

JGR

Journal of Geophysical Research: Space Physics

RESEARCH ARTICLE
10.1002/2014JA020787

Key Points:
- P_{SW}, energy loading, and sunspot number are factors affecting growth phase pressure
- Model well predicts observed pressure and pressure gradients
- Model helps understand the observed temporal and spatial pressure variations

Correspondence to:
C. Yue,
yuechao@atmos.ucla.edu

Citation:
Yue, C., C.-P. Wang, L. Lyons, Y. Wang, T.-S. Hsu, M. Henderson, V. Angelopoulos, A. T. Y. Lui, and T. Nagai (2015), A 2-D empirical plasma sheet pressure model for substorm growth phase using the Support Vector Regression Machine, *J. Geophys. Res. Space Physics, 120*, doi:10.1002/2014JA020787.

Received 1 NOV 2014
Accepted 13 FEB 2015
Accepted article online 17 FEB 2015

A 2-D empirical plasma sheet pressure model for substorm growth phase using the Support Vector Regression Machine

Chao Yue[1], Chih-Ping Wang[1], Larry Lyons[1], Yongli Wang[2], Tung-Shin Hsu[3], Michael Henderson[4], Vassilis Angelopoulos[3], A. T. Y. Lui[5], and Tsugunobu Nagai[6]

[1]Department of Atmospheric and Oceanic Sciences, University of California, Los Angeles, California, USA, [2]Goddard Planetary Heliophysics Institute, University of Maryland, Baltimore County, Baltimore County, Maryland, USA, [3]Department of Earth and Space Sciences, University of California, Los Angeles, California, USA, [4]Space Science and Applications, Los Alamos National Laboratory, Los Alamos, New Mexico, USA, [5]Applied Physics Laboratory, Johns Hopkins University, Laurel, Maryland, USA, [6]Department of Earth and Planetary Sciences, Tokyo Institute of Technology, Tokyo, Japan

Abstract The plasma sheet pressure and its spatial structure during the substorm growth phase are crucial to understanding the development and initiation of substorms. In this paper, we first statistically analyzed the growth phase pressures using Geotail and Time History of Events and Macroscale Interactions during Substorms data and identified that solar wind dynamic pressure (P_{SW}), energy loading, and sunspot number as the three primary factors controlling the growth phase pressure change. We then constructed a 2-D equatorial empirical pressure model and an error model within $r \leq 20\,R_E$ using the Support Vector Regression Machine with the three factors as input. The model predicts the plasma sheet pressure accurately with median errors of 5%, and predicted pressure gradients agree reasonably well with observed gradients obtained from two-probe measurements. The model shows that pressure increases linearly as P_{SW} increases, and the P_{SW} effect is stronger under lower energy loading. However, the pressure responses to energy loading and sunspot number are nonlinear. The pressure increases first with increasing loading or sunspot number, then remains relatively constant after reaching a peak value at ~8000 kV min loading or sunspot number of ~80. The loading effect is stronger when P_{SW} is lower and the pressure variations are stronger near midnight than away from midnight. The sunspot number effect is clearer at smaller r. The pressure model can also be applied to understand the pressure changes observed during a substorm event by providing evaluations of the effects of energy loading and P_{SW}, as well as the temporal and spatial effects along the spacecraft trajectory.

1. Introduction

The plasma sheet pressure and its spatial variation are important to understanding plasma sheet dynamics, since they reflect the changes in particle energization and magnetic field configurations. The energy input from the solar wind energizes the plasma sheet particles and at the same time the magnetic field reconfigures to maintain force balance with the changing plasma pressure. Increasing radial plasma pressure gradients cause stretching of magnetic field lines, while azimuthal pressure gradients result in bending of magnetic field lines. Understanding the plasma sheet pressure evolution is particularly important to substorms since there is continuous (~20 to 60 min) and enhanced solar wind energy input during the substorm growth phase [*McPherron,* 1970], and the resulting pressure increases [e.g., *Baker and McPherron*, 1990], and stretched magnetic field configurations in the near-Earth plasma sheet [e.g., *Sergeev et al.*, 1990, 2011; *Sanny et al.*, 1994] are believed to be crucial to the onset of the expansion phase. For example, they may become favorable to ballooning instability [e.g., *Miura et al.,* 1989; *Liu,* 1997; *Pu et al.,* 1997]. There are several factors that control the pressure distribution and its evolution during the substorm growth phase, which limits our ability to understand its evolution from individual satellite observations. Our goal thus is to take advantage of multiyears of spacecraft data to determine the factors that are well correlated with plasma sheet pressure and to use these as control factors to model the pressure distribution in order to better understand its influence on magnetospheric dynamics.

Large-scale distributions of the plasma sheet pressure and their dependencies on the solar wind condition and geomagnetic activity have been studied using in situ measurements in the magnetosphere. The pressure is reported to increase with decreasing distance to the Earth for all levels of activity [*Angelopoulos et al.,* 1993; *Angelopoulos,* 1996]. Away from the central plasma sheet, the plasma pressure decreases while the magnetic

pressure increases to balance each other [*Fairfield et al.*, 1981; *Baumjohann et al.*, 1990; *C.-P. Wang et al.*, 2013; *Y. Wang et al.*, 2013]. *Spence et al.* [1989] showed that the pressure magnitudes and their earthward gradients increase with increasing *Kp*. *Tsyganenko and Mukai* [2003] established a 2-D empirical plasma pressure model based on Geotail data in the region of $r = 10$ to 50 R_E, controlled by the interplanetary magnetic field (IMF) and solar wind dynamic pressure (P_{SW}). Their results showed that there is no significant dawn-dusk pressure asymmetry, in line with the observed symmetry of the tail lobe magnetic fields. In addition, *Wang et al.* [2006] investigated how pressure profiles change with IMF B_Z history by using Geotail data and their results showed that the overall pressure magnitude is higher when IMF has been dominantly southward for a longer period. Their results also showed a very weak dawn-dusk asymmetry. Furthermore, *Wang et al.* [2009] showed that the equatorial plasma pressure increases everywhere as the cross polar cap potential or *AE* increases. Additionally, the plasma sheet pressure is also well correlated with the P_{SW} with higher pressure under higher P_{SW} [e.g., *Borovsky et al.*, 1998; *C.-P. Wang et al.*, 2013; *Y. Wang et al.*, 2013]. Since the plasma pressure distributions depend on various factors, it is important to understand quantitatively how the pressure changes in response to changes in these factors.

There have been only a few studies focusing on the pressure changes during substorms. *Miyashita et al.* [2000, 2001, 2003, 2009, 2010] studied the equatorial pressure and magnetic field variations around the substorm onset based on Geotail observations and found that pressure increases earthward of 12 R_E 2 min before onset while it decreases tailward of the initial dipolarization region. Similar results were found by *Xing et al.* [2010]. In addition, *Xing et al.* [2011] used simultaneous measurements from two Time History of Events and Macroscale Interactions during Substorms (THEMIS) probes to obtain azimuthal pressure gradients and showed that a westward azimuthal pressure gradient is enhanced before onset at $r \sim 11$ R_E. Furthermore, *Wing et al.* [2007] investigated the DMSP observations of ion pressures at the low-altitude ends of the plasma sheet and found that the pressure peaks at the inner edge of the plasma sheet during the substorm growth phase. Also, *Machida et al.* [2009] investigated the temporal development of the near-Earth magnetotail during substorms by conducting multidimensional superposed-epoch analysis of Geotail data. They showed that the total pressure starts to decrease around $X = -16$ R_E about 4 min before the substorm onset, and the decrease then propagates both earthward and tailward along the lobes, consistent with the results from *Miyashita et al.* [2009].

These previous studies have provided some general understanding about how pressure changes during the growth phase. However, how the pressure and its spatial variations are correlated with the intensity of a substorm and how they are affected by factors of the solar wind condition and geomagnetic activity, which are different for each substorm, remain to be determined. The objective of this study is thus to use a large observational data set from Geotail and THEMIS and a Support Vector Regression Machine (SVRM) technique to construct empirical pressure model that allows us to quantitatively determine the changes in large-scale equatorial plasma sheet pressure distributions during the growth phase in response to different factors. SVRM is regression analysis with machine-learning techniques. Unlike the previous plasma sheet empirical pressure models [*Spence and Kivelson*, 1993; *Tsyganenko and Mukai*, 2003; *C.-P. Wang et al.*, 2013; *Y. Wang et al.*, 2013] that used analytical forms, SVRM requires no pre-assumed function forms and is suitable for analyzing systematic responses to driving factors that are likely to interact with each other. SVRM has been successfully applied by *Y. Wang et al.* [2013], in modeling the 3-D magnetopause shape. They used a magnetopause-crossing database from multiple satellite observations to construct a new 3-D magnetopause model with the shape of the magnetopause, including its cusps and complex dependence on various control parameters, automatically determined by using SVRM, and they achieved very high prediction accuracy compared with observed data, which is not guaranteed by the previous magnetopause models.

This paper is organized as follows: the observational data and the factors that are well correlated with the pressure during substorm growth phase are described in section 2. The principle of SVRM, pressure model construction, and model validation are presented in section 3. Section 4 describes the main results of our pressure model and an application to one substorm case. Section 5 summarizes our main findings.

2. Plasma Pressure During the Substorm Growth Phase

2.1. Observational Data

In this study, we investigate pressure during substorm growth phase measured by Geotail from 1995 to 2005 and by THEMIS from 2007 to 2010. We used a substorm list from *Hsu and McPherron* [2012]. The onset of each

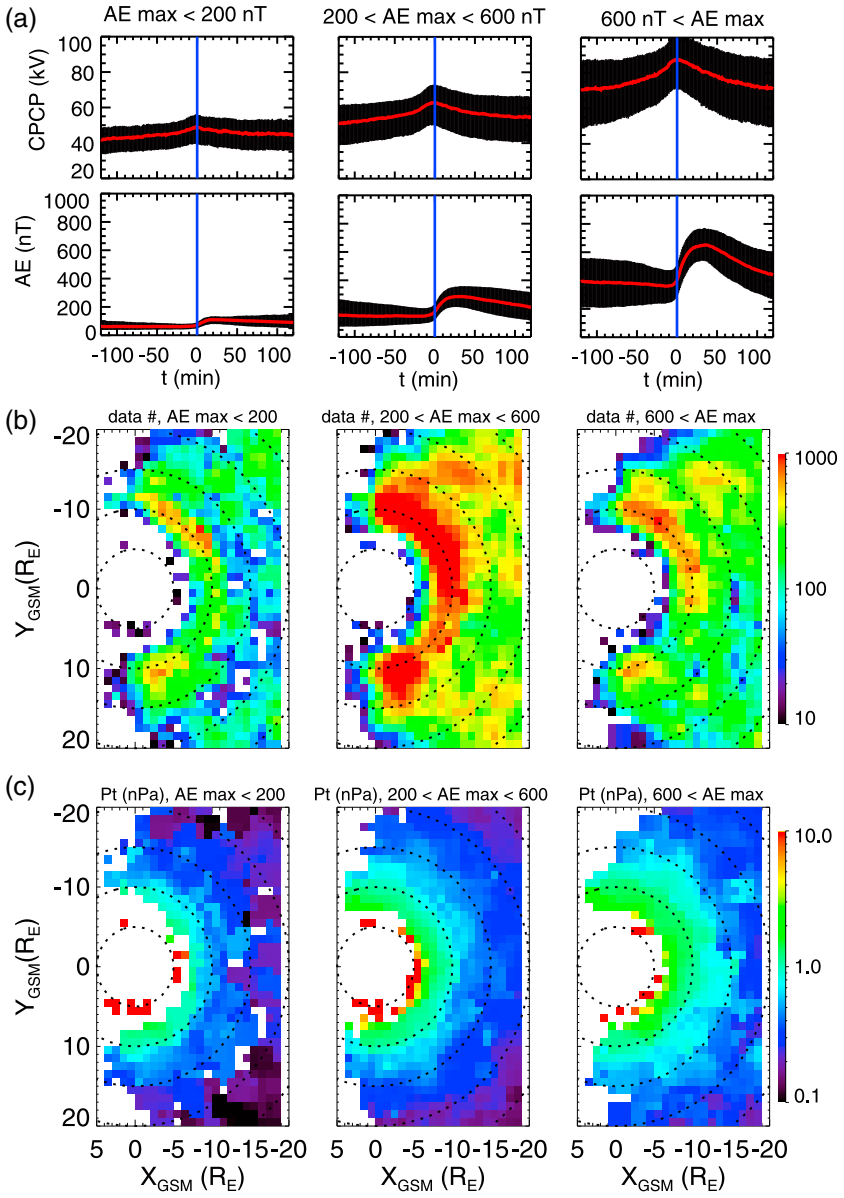

Figure 1. The statistical results for three different intensity of substorms (*AE* max < 0 nT; 200 nT < *AE* max < 600 nT; 600 nT < *AE* max). (a) CPCP and *AE* variations in 2 h prior to and 2 h after substorm onset. The vertical blue lines make the substorm onset time. The red line is the median value, and the upper and lower bounds are the upper and lower quartiles. (b) The data points and (c) plasma sheet pressure distributions during substorm growth phase (0–60 min before onset).

substorm was identified by a sharp drop in *AL* index (more than 100 nT in 20 min). There are more than 20,000 substorms thus identified from 1995 to 2010. The plasma pressure data during the substorm growth phase (here we assume that the substorm growth phase is the 60 min period before an onset) are then collected. Plasma data from two instruments aboard Geotail are used: the ion and electron data from the low-energy particle (LEP) instrument [*Mukai et al.,* 1994] that covers the ion energy range from 21 eV/q to 44 keV/q and the electron energy range from 43 eV to 41 keV, and the proton data from the energetic particles and ion composition (EPIC) instrument [*Williams et al.,* 1994] that covers the ion energy range from 46 to 3005 keV (EPIC only measures 32 and >110 keV integral electrons, so electron moments are not available). The ion pressures are a summation of the LEP and EPIC data, while the electron pressures are from the LEP data only. One minute average of the Geotail plasma data is used. For THEMIS, the ions and electrons are measured by an

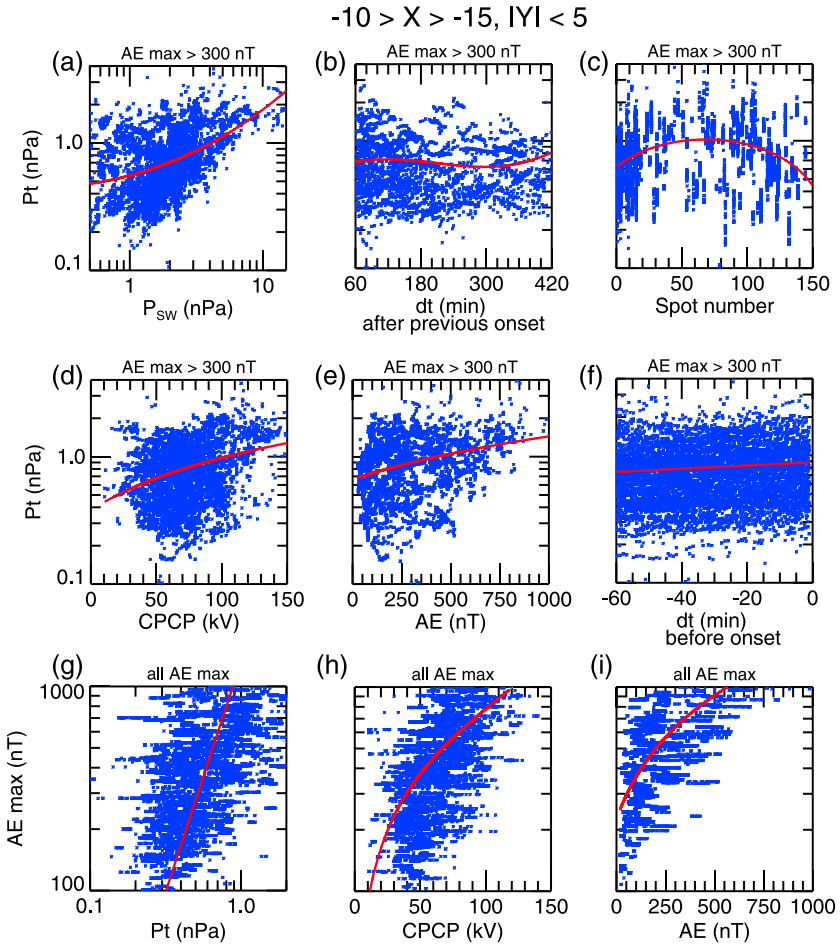

Figure 2. (a–f) Plasma sheet pressures during substorm growth phase (0–60 min before onset) as functions of P_{SW}, the time since previous substorm, the sunspot number, CPCP, *AE*, and the time before the substorm onset at region of $-10 < X_{GSM} < -15\ R_E$ and $-5 < Y_{GSM} < 5\ R_E$ for substorms that *AE* max > 300 nT. (g–i) *AE* max as functions of plasma sheet pressure, CPCP, and the *AE* index during substorm growth phase (0–60 min before onset) at region of $-10 < X_{GSM} < -15\ R_E$ and $-5 < Y_{GSM} < 5\ R_E$. The red line in each panel is the linear or polynomial fitting curve.

electrostatic analyzer (ESA, 0.006–20 keV/q for ions and 0.007–26 keV for electrons) [*McFadden et al.*, 2008] and a solid state telescope (SST, 35 keV–6 MeV for ions and 30 keV–6 MeV for electrons). Full distributions are used with time resolution of a few minutes. The plasma pressures are a summation of the ESA and SST pressures. For both Geotail and THEMIS, total plasma pressure is a summation of ion and electron plasma pressure. The plasma pressure is assumed isotropic. Magnetic field data are from the Geotail magnetic field experiment [*Kokubun et al.*, 1994] and the THEMIS Fluxgate Magnetometer (FGM) instrument [*Auster et al.*, 2008]. Aberrated geocentric solar magnetospheric (GSM) coordinates (with the aberration angle determined by 1 h averaged solar wind velocity) are used for both THEMIS and Geotail data. In this study, our interest is the plasma pressure on the equatorial plane. As demonstrated in *C.-P. Wang et al.* [2013], *Y. Wang et al.* [2013], from the force balance equation $\nabla \mathbf{P}_p = 1/\mu_0(\nabla \times \mathbf{B}) \times \mathbf{B}$, in the *Z* direction, one can obtain $P_P + P_B, r - 1/\mu_0 \int_0^z ((\partial Bz/\partial x \cdot Bx + \partial Bz/\partial y \cdot By)\mathrm{d}z) = P_{p,\mathrm{eq}}$, where $P_{B,r} = (Bx^2 + By^2)/2\mu_0$ is the radial magnetic pressure and $1/\mu_0 \int_0^z ((\partial Bz/\partial x \cdot Bx + \partial Bz/\partial y \cdot By)\mathrm{d}z)$ is the magnetic curvature term. If the magnetic curvature term is 0, then total pressure $Pt = P_p + P_{B,r} = P_{p,\mathrm{eq.}}$ at a fixed (*X*, *Y*) location should be a constant along the *Z* direction and its value equals the pressure at the equatorial plane, thus is independent of the plasma beta. In the plasma sheet, the magnetic curvature term is generally small in the vicinity of the current sheet. Therefore, we use total pressure *Pt* instead of plasma pressure P_p to represent the plasma pressure on the equatorial plane when a satellite is off the equator.

2.2. Factors Controlling the Growth Phase Pressure

Figure 1a shows the statistical results of cross polar cap potential drop (CPCP; calculated by using Weimer model [*Weimer,* 1995]) and *AE* variations in 2 h prior to and 2 h after substorms onset for three ranges of substorm intensity (in this study, we use the maximum *AE* value, *AE* max, during the 40 min period after an onset to indicate the intensity of a substorm). The median values of CPCP and *AE* increase as increasing substorm intensity. CPCP gradually increases while *AE* shows little change during substorm growth phase. And CPCP peaks around the substorm onset then gradually decays. While *AE* shows a step increase after onset, peaking around 30 min later, it then gradually decays. Figures 1b and 1c show the number of data points and the corresponding equatorial medians of the growth phase pressure distributions for the same three different substorm intensities as shown in Figure 1a. Only data points with plasma beta, P_P/P_B, larger than 1 were used (total ~1,250,000 points). It can be seen that the overall pressure is higher for more intense substorm. To find out what factors can be related to a larger increase in plasma sheet pressure during the growth phase to result in a more intense substorm, we investigated how the growth phase pressure is correlated with different solar wind parameters and with the time since a previous substorm.

Figures 2a–2f show growth phase pressure (only data points with beta >1 and corresponding *AE* max >300 nT) and the corresponding linear or polynomial fitting curve (red line) at region of $-10\leq X\leq -15\ R_E$ and $|Y|\leq 5\ R_E$ as a function of P_{SW}, the time duration from the onset of the previous substorm, the observed monthly averaged sunspot number, 30 min average (over the 30 min period prior to each pressure data point) of CPCP, 30 min average of *AE*, and the time before the substorm onset. The sunspot number is considered since our data set spans over one solar cycle. The pressure is seen to increase with increasing P_{SW}, CPCP, and *AE* in general as indicated by the fitting curves. The correlation between pressure and the time since a previous onset is weak as shown by the red fitting curve, whereas the upper bound of pressure is higher when the time since a previous substorm is shorter, that is, when the growth phase of this substorm starts in earlier recovery phase of the previous substorm, indicating the higher pressure is partially due to the energy that was loaded during the growth phase of the previous substorm but was not dissipated during that substorm. This correlation with the previous substorm is reflected on the correlation with *AE* shown in Figure 2e. Since *AE* reaches a peak during the expansion phase then decreases in the recovery phase, a growth phase that starts within the recovery phase of the previous substorm corresponds to larger *AE* than does a growth phase well separated from the previous substorm. Thus, the *AE* values during a growth phase can be used as a proxy to indicate the energy that was loaded during the previous substorm and still remains in the plasma sheet. The pressure increases first and then decreases with sunspot number, showing a peak at sunspot number of ~80 as seen from the red curve. On the other hand, the pressure shows little correlation with the time duration before the substorm onset statistically because of the very different temporal variations of CPCP, *AE*, and P_{SW} seen in each substorm. Figures 2g–2i show the *AE* max and the corresponding linear or polynomial fitting curve (red line) as a function of growth phase pressure and 30 min averages of CPCP and *AE*. The *AE* max increases as plasma pressure or CPCP or *AE* increases, indicating that higher plasma sheet pressure, in response to larger solar wind energy input and/or larger energy remaining from the previous substorm, results in a more intense substorm.

As shown in Figure 2, the plasma sheet pressure is highly correlated with CPCP and *AE*. However, instantaneous CPCP or *AE* value cannot uniquely determine the state of energy input from the solar wind or the energy remained from the previous substorm. First of all, while convection strength does determine the rate of energy loading, it does not uniquely specify the state of energy loading, which depends on the time history. For example, the plasma sheet pressure might keep increasing even though CPCP is enhanced but remains constant. In addition, the CPCP or *AE* temporal variation during the substorm growth phase can be very different case by case, which can readily be seen in the many events we have examined. The CPCP or *AE* may increase or decrease gradually, have almost no change, or fluctuate a lot during the substorm growth phase. To consider the effect of history, we defined two energy loading parameters that are the time integrals of CPCP and *AE*, that is, PCP energy loading $\left(\int_{t1}^{t}\mathrm{PCP}\cdot dt\right)$ and *AE* energy loading $\left(\int_{t1}^{t}AE\cdot dt\right)$, where the integral is over time from a chosen time t_1 before onset to the time t. We have tested $t_1=30$, 60 and 90 min and found that the energy loading parameters with $t_1=60$ min are best correlated with the *AE* max. We also created a new energy loading parameter that combines the two loadings, that is, PCPAE energy loading = PCP loading + $4/25\cdot AE$ loading. The weighting factor 4/25 gives the range of *AE* loading to be the same as range as the PCP loading

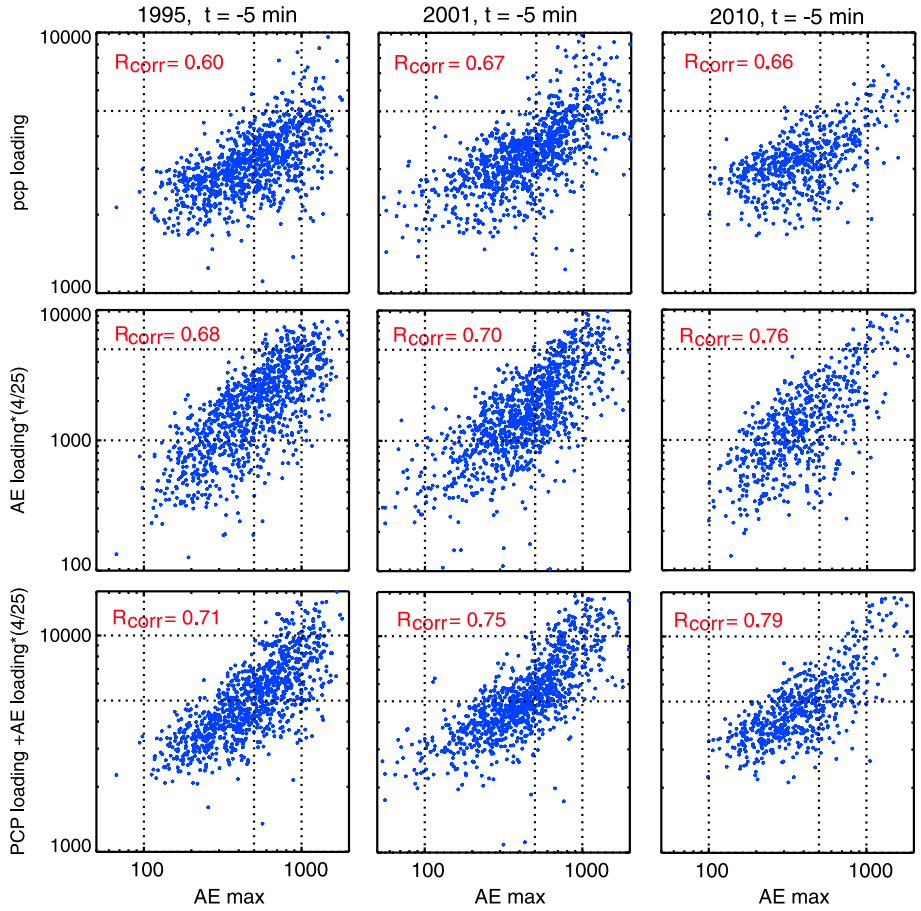

Figure 3. Illustration of the linear correlations between the *AE* max and the PCP loading, *AE* loading as well as PCPAE loading at 5 min before substorm onset for the years 1995, 2001, and 2010.

range, and thus gives the *AE* loading an equal weight to the PCP loading. We tested different weighting factors and found that 4/25 has the highest correlations with *AE* max. The units of PCPAE energy loading are kV min.

Figure 3 shows the correlations between the *AE* max and the three energy loading parameters during different stages of a solar cycle (1995 and 2010 are near a solar minimum and 2001 is near a solar maximum). It can be seen that the linear correlation coefficients are always the highest for the PCPAE loading. Thus, in the following analysis, we use the PCPAE loading parameter as the energy loading factor, instead of using PCP

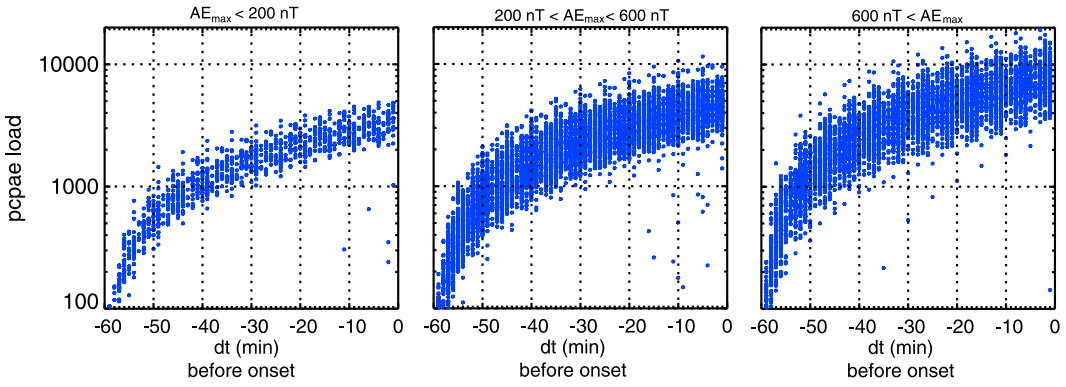

Figure 4. PCPAE loading variation during substorm growth phase (60 min substorm growth phase duration) for small substorms (*AE* max < 200 nT), moderate substorms (200 < *AE* max < 600 nT), and intense substorms (600 nT < *AE* max).

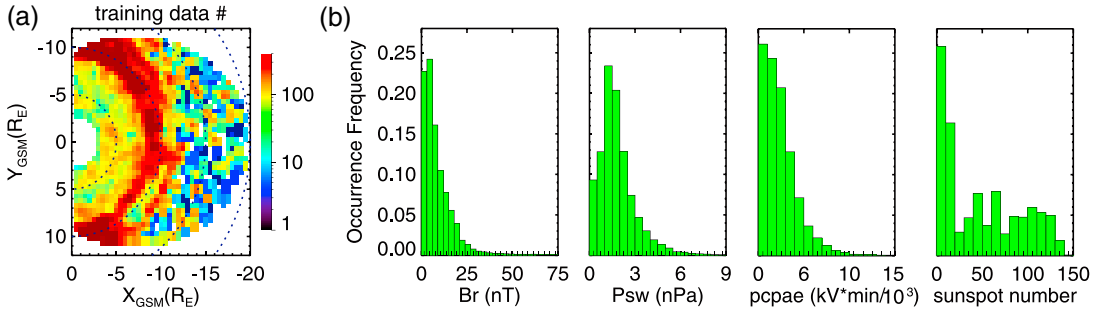

Figure 5. (a) Distribution of the pressure fitting data points on the equatorial plane inside the area we interested. (b) Distributions of four control parameters (*Br*, P_{SW}, PCPAE loading, and sunspot numbers) for pressure fitting.

and *AE* as separate loading parameters. Figure 4 shows the temporal variations of the PCPAE energy loading during the substorm growth phase for three different *AE* max ranges. The PCPAE loading increases as the growth phase proceeds. For larger *AE* max, the PCPAE loading at the beginning of the growth phase is higher, which is likely due to higher *AE* values resulting from the previous substorm. The PCPAE loading also increases more quickly and reaches a higher value before the onset for more intense substorms.

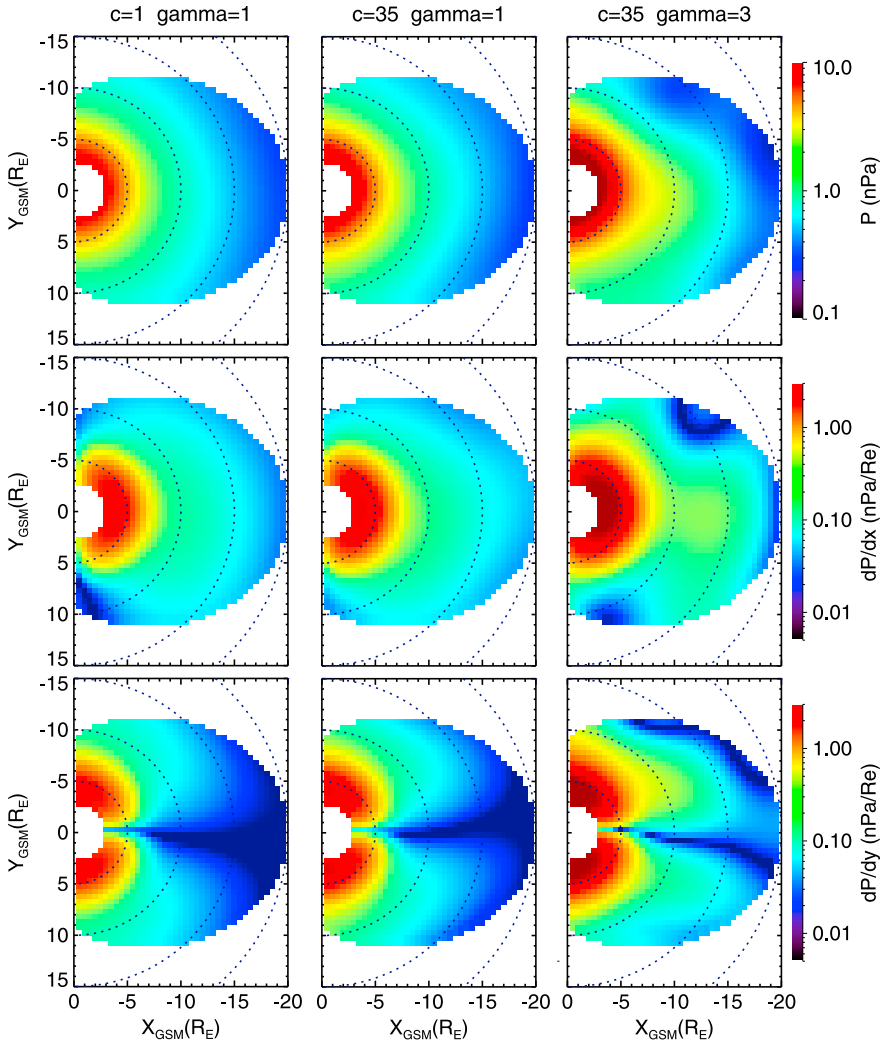

Figure 6. Equatorial distributions of plasma pressure, pressure gradient in direction of X_{GSM} and Y_{GSM} coordinates for different C and γ choices.

3. Regression Analysis and Empirical Pressure Model

To quantitatively understand how the three primary factors identified in section 2, PCPAE loading, P_{SW}, and the sunspot number control the plasma sheet pressure during substorm growth phase, we conduct regression analysis using a Support Vector Regression Machine (SVRM) technique. This allows us to construct a SVRM empirical pressure model to evaluate the plasma pressure changes in response to each of these factors. In the analysis, we consider the plasma pressure data locations in *X* and *Y*, and use *Br* to indicate the relative *Z* distance to the equatorial plane ($Br = 0$).

3.1. Support Vector Regression Machine

SVRM is regression analysis using the Support Vector Machine (SVM) [*Drucker et al.*, 1997]. SVM is a supervised machine-learning technique in the framework of statistical learning theory [*Vapnik and Lerner*, 1963; *Noble*, 2006]. The SVRM maps multidimensional data (in this study, *X*, *Y*, *Br*, P_{SW}, PCPAE loading, and sunspot number) into a high-dimensional feature space (plasma pressure in this study), via nonlinear mapping through a selected kernel function, and performs a linear regression in this space. SVRM is nonparametric, thus requiring no analytical forms for the model. In contrast, previous plasma sheet pressure models, such as *Spence and Kivelson* [1993], *Tsyganenko and Mukai* [2003], and *C.-P. Wang et al.* [2013], *Y. Wang et al.* [2013], are parametric and analytical forms are specified. These parametric models require a large database to achieve reasonable accuracy, and the forms may not be sufficiently flexible to well represent the observed distributions of plasma sheet pressure. Compared with parametric analysis, the SVRM technique is expected to be more efficient since it can incorporate many types of high-dimensional, multiscale input data, which is always problematic for parametric analysis. SVRM also avoids the traps of local minima, and it theoretically does not suffer "the curse of dimensionality," which is a problem for parametric models when available data become sparse as the dimensionality increases. There have been some studies in space physics successfully using SVM for forecasting. For example, *Gavrishchaka and Ganguli* [2001] used SVM to predict *AE* index from solar wind and IMF data and they concluded that their *AE* model gives a reliable prediction of large-amplitude substorm events. An empirical model for predicting low-latitude storm time ionospheric f_oF_2 using the SVM technique was developed by *Ban et al.* [2011], and their results indicated that the model can capture the low-latitude ionospheric disturbances most of the time. *Liu et al.* [2011] predicted the hourly average solar wind velocity with SVM and found that the predicted velocity values are very close to the observations for most of the time, indicating that their SVM prediction is accurate and reliable. Furthermore, *Huang et al.* [2009] used SVM to forecast daily $F_{10.7}$ index and found that their model can perform well with only a small fitting database.

In this study, we have used LibSVM (version 3.17), a freely available and widely used implementation of SVRM, which handles all the complex technical details for this technique [*Chang and Lin*, 2001]. Details of how to use LibSVM can be found in *Y. Wang et al.* [2013]. In LibSVM, different SVM types and kernel functions are supported. We chose the commonly used epsilon-SVR and Radial Basis Function (RBF), $\exp(-\gamma|u-v|^2)$, where u is data, v is prediction, and γ controls how far a discrete data point is effective in constructing a continuous fitted parameter function for fitting in the high-dimensional feature space. This combination is very flexible and robust in handling many problems and is free from many difficulties of some other combinations. The RBF is used first to map our data to high-dimensional feature space. Then in this feature space, SVR is used to obtain a smooth model surface.

3.2. Constructing SVRM Empirical Plasma Pressure Model

We randomly selected 100,000 data points within the plasma sheet (defined here by requiring $Br/B_Z \leq 1$) for SVRM fitting. Adding more model fitting data will consume more computing resources since the complexity of SVRM fitting is quadratic of the number of fitting data. We chose 100,000 data points to do model fitting to balance the computational burden and model accuracy. The distributions of the selected data points are shown in Figure 5a, with more data points located in the transition region where the magnetic field configuration changes from dipole-like to taillike configuration around $r \sim 7$ to $12\,R_E$ than at other locations. As shown in Figure 5b, the majority of the data points correspond to *Br* between 0 and 30 nT, P_{SW} between 0 and 6 nPa, PCPAE loading between 0 and 10,000 kV min, and the sunspot number between 0 and 140. Therefore, SVRM predictions outside these ranges may not be as reliable as those within the ranges.

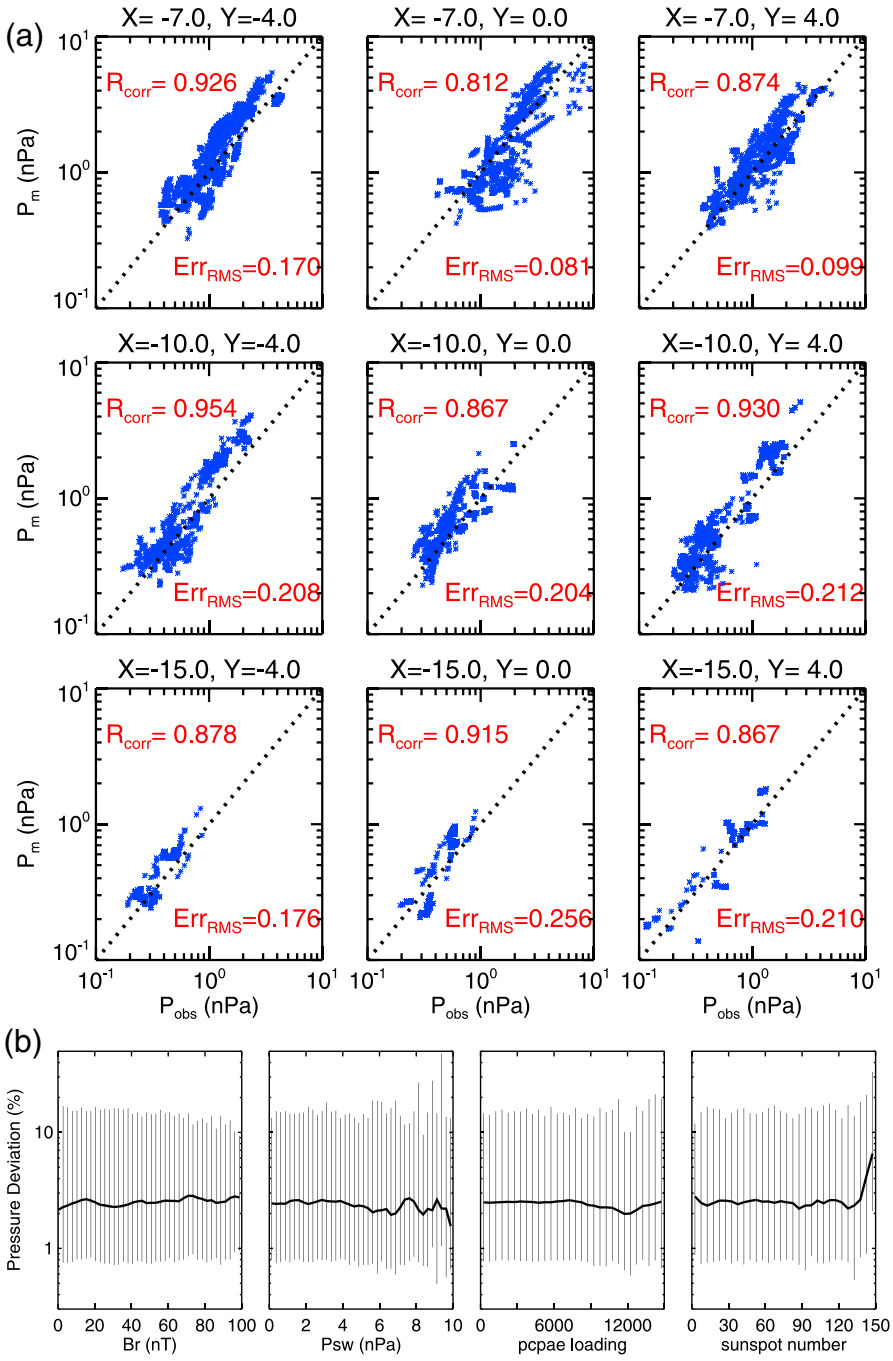

Figure 7. (a) The comparison of modeled and observed pressures at different locations. R_{corr} is the linear correlation coefficient between P_m and P_{obs}. Err_{RMS} is the normalized root-mean-square (RMS) error. (b) The statistical results of normalized deviations between the modeled and observed pressures as functions of *Br*, P_{SW}, PCPAE loading, and sunspot number. The black solid lines are the median values, and the errors are the lower and upper quartiles.

There are three free parameters (α, *C*, and γ) in the model fitting process. The parameter α, introduced through SVR, is the distance from the fitted surface within which no fitting error is counted for a data point. Here we set $\alpha = 0$, thereby requiring the fitted surfaces to go through the center of the data distributions as much as possible. The error factor, *C*, introduced through SVR, is defined for data points falling outside of distance α, and γ is the parameter in RBF. Using different *C* and γ, SVRM gives different model pressure distributions. A larger γ leads to a smaller data effective range and the model reflects more local observations.

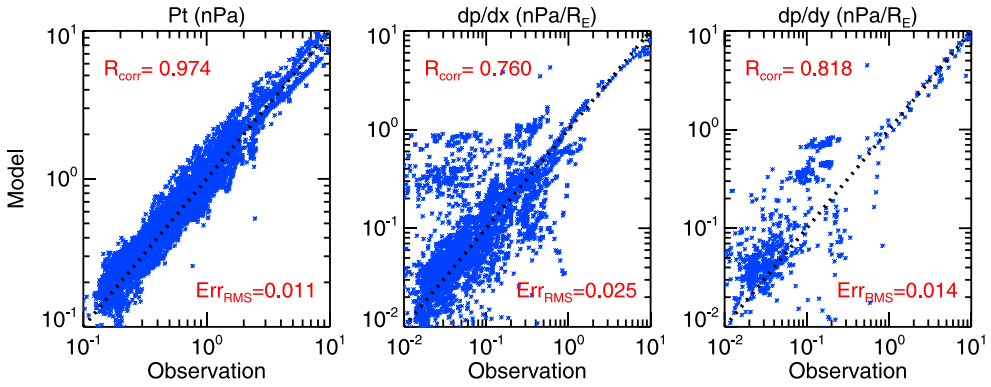

Figure 8. Comparison of the modeled and the observed pressures and pressure gradients in directions of X_{GSM} and Y_{GSM}. R_{corr} is the linear correlation coefficient between P_m and P_{obs}. Err_{RMS} is the normalized RMS error.

And a larger C leads to tighter fitting of the data points, which can adversely affect model smoothness. The choices for C and γ are critical to guarantee the regression effectiveness. To reduce the computation complexity, we first performed a coarse grid search (γ is from 0.001 to 10 and C is from 0.01 to 300) to identify a region that includes the optimal combination of C and γ. We then conducted a fine grid search with a unit grid of C from 1 to 40 and γ from 1 to 4. We found that using $\gamma = 1$ and $C = 1$ yields the best regression accuracy, as is shown later in the comparisons between model pressures and observations. Figure 6 shows three examples of the model equatorial plasma pressure and the pressure gradients along the X and Y directions for ($\gamma = 1$, $C = 1$), ($\gamma = 1$, $C = 35$), and ($\gamma = 3$, $C = 35$) with $Br = 0$, $P_{SW} = 2$ nPa, PCPAE loading = 4000 kV min, and sunspot number = 50. Clearly, there are more bumpy pressure and pressure gradient structures with a larger γ or C, which reflects more the local small-scale variations, although the difference between different C values is not as strong as γ. Therefore, we chose $\gamma = 1$ and $C = 1$ for our pressure model for its accuracy and for giving smooth large-scale structures.

To provide error estimation of the pressure predictions from the model ($\gamma = 1$ and $C = 1$), we constructed a SVRM error model using the same control parameters (X, Y, Br, P_{SW}, PCPAE loading, and sunspot number). It enables us to obtain model errors appropriate to different locations and control parameters. Instead of fitting the pressure, we fitted the normalized deviations ($|P_{obs} - P_m|/P_{obs}$) between our model pressures (P_m) and the 10,000 observation data points (P_{obs}) used in the pressure model fitting. We assumed $\alpha = 0$, and searched a unit grid of γ from 1 to 4 and C from 1 to 40. Again, the ending search values of γ and C were determined after trials. We checked model results for the same set of standard control parameters of $Br = 0$, $P_{SW} = 2$ nPa, PCPAE loading = 4000 kV min, and sunspot number = 50, and chose $\gamma = 1$ and C = 1 for the final error model, which gives error model accuracy and smoothness as for the pressure model.

3.3. Model Validation

After we established the pressure model and error model, we further verify the model performance by comparing observations selected from the database of ~2,800,000 data points with model predictions with inputs from the loading, P_{SW}, and the sunspot number corresponding to each observation point. Figure 7a shows the comparisons of model pressures with the observed ones at different locations near the equatorial plane. Here we selected the data to be close to the equatorial plane by requiring $Br/B_Z \leq 1$. As we can see, the predicted pressures match well with the observed ones in general. Figure 7b shows the deviations between the model and observed pressure as a function of Br, P_{SW}, PCPAE loading, and sunspot number of the 2,800,000 data points. The black lines show the median values of pressure deviations, which are less than 5% for all situations, and the upper quartiles are mostly less than 20%. Meanwhile, the pressure deviations show almost no change with Br, P_{SW}, PCPAE loading, and sunspot number, except for the larger deviations when the sunspot number is larger than ~135.

We further verified whether the predicted pressure structures can provide reliable pressure gradients by comparing them with the observed pressure gradients computed from simultaneous measurements from two THEMIS probes. We searched an aurora substorm list [*Nishimura et al.*, 2011] and found about 200 cases having either a good radial or azimuthal conjunction between two THEMIS probes so that we are able to

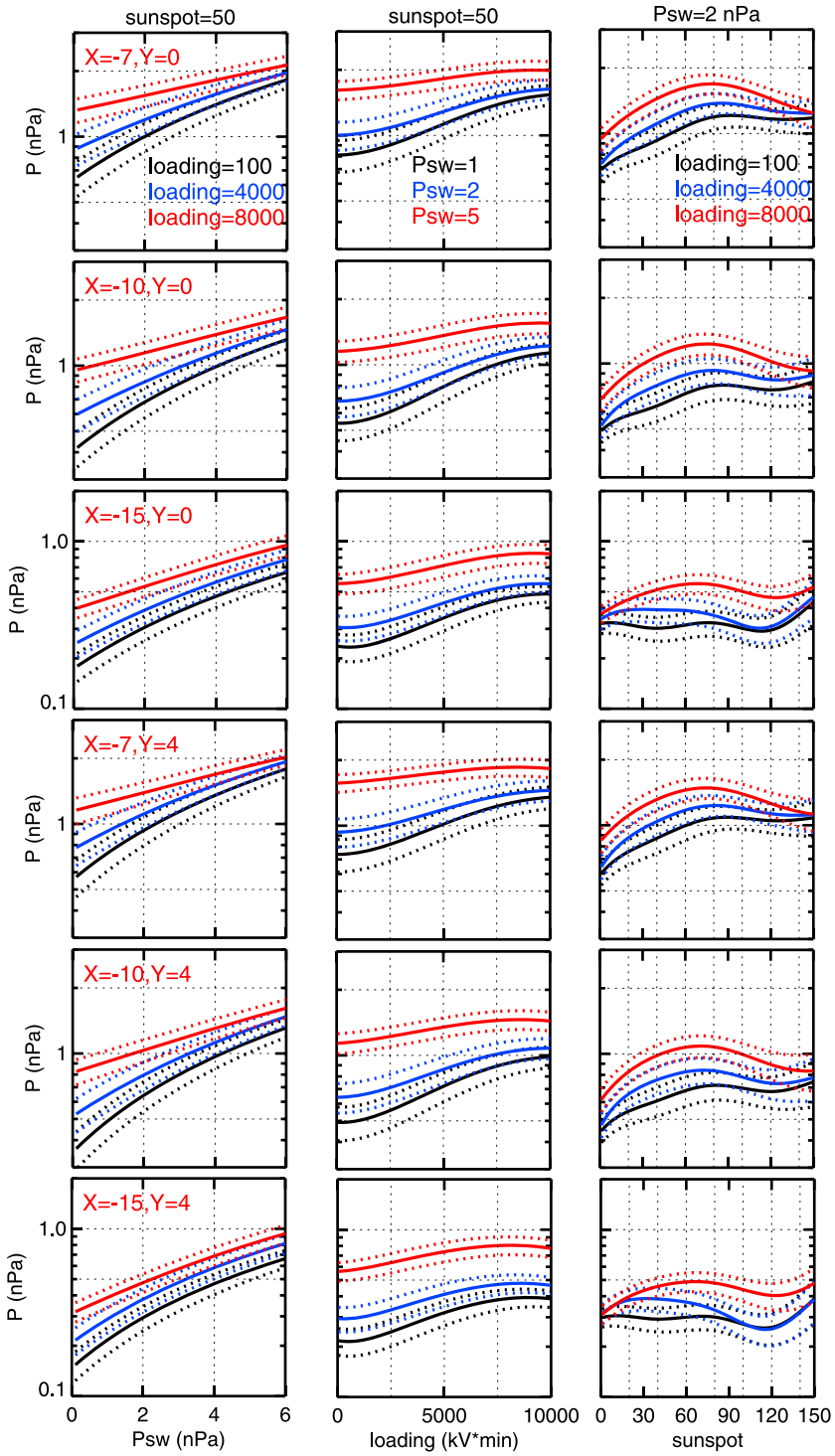

Figure 9. The modeled equatorial ($Br = 0$) pressures and their error bounds at different radial distance of premidnight and midnight meridian as functions of P_{SW}, PCPAE loading, and sunspot number within their reliable ranges. (left column) The red, blue, and black lines represent PCPAE loading at 100, 4000, and 8000 kV min, respectively, and sunspot number = 50 for all cases. (middle column) The red, blue, and black lines represent P_{SW} equals 1, 2, and 5 nPa, respectively, and sunspot number = 50 for all cases. (right column) The red, blue, and black lines represent PCPAE loading at 100, 4000, and 8000, respectively, and $P_{SW} = 2$ nPa for all cases.

compute directly pressure gradients. Figure 8 shows the comparisons of pressure and the magnitudes of pressure gradients in the X direction (requiring the probe separation $|dY| < 1\ R_E$ and $|dX|/|dY| > 2$) and Y direction (requiring the probe separation $|dX| < 1\ R_E$ and $|dY|/|dX| > 2$) between the THEMIS observations and predictions. We selected data points within the plasma sheet by requiring data having plasma beta > 0.1 for $r < 7\ R_E$ and beta > 0.6 for $r = 7$ to $10\ R_E$ and beta > 1 for $r > 10\ R_E$. In general, the predicted pressures are highly correlated with the observations and the majority of the predicted pressure gradients match well the observations. The above two validations indicate that our SVRM model can reliably allow us to evaluate quantitatively the individual and combined effects from energy loading, P_{SW}, and the sunspot number on the large-scale plasma sheet distributions during the substorm growth phase.

4. Results of the Empirical Pressure Model

4.1. Effect of P_{SW}, Energy Loading, and Sunspot Number

Figure 9 shows how the pressures and error bounds predicted by the pressure model and error model change as P_{SW}, PCPAE loading, or sunspot number increases within its reliable ranges while the other two parameters are constant. Results are shown at different X distances along midnight and along $Y = 4\ R_E$. It can be seen in the left column that under a fixed energy loading, the model pressure increases linearly as P_{SW} increases at all locations, and the increase is stronger when the corresponding energy loading is lower. These dependences are likely a result of the balance between P_{SW} and magnetosphere pressure (magnetic pressure in the lobes and plasma pressure on the equatorial plane). For example, when equatorial plasma pressure becomes higher due to higher energy loading, the resulting stronger lobe magnetic pressure makes it more difficult for P_{SW} to compress the magnetosphere, as indicated by the studies of *Petrinec and Russell* [1993] and *Shue et al.* [1997] showing that the nightside magnetopause size under the same P_{SW} is larger when IMF Bz is more negative.

As shown in the middle column, the model pressure under a fixed P_{SW} increases nonlinearly as energy loading increases. The pressure increases first with increasing energy loading then becomes relatively constant after loading reaches ~8000–10,000 kV min. The pressure increase with energy loading is relatively larger when the corresponding P_{SW} is lower, which is also likely the result of the balance between the P_{SW} and magnetosphere pressure discussed above. In addition, the pressure increase with increasing energy loading is larger near midnight than away from midnight. This may be the result of two factors. The PCPAE energy loading includes both effects from convection (PCP loading) and the previous substorm (*AE* loading). The pressure change due to particle energization under earthward convection strongly depends on the distributions of Bz. Typically, the magnitude of the equatorial Bz minimizes near midnight and $|dBz/dX|$ is the largest along the $Y = 0$ line (for example, see the equatorial Bz profiles shown in Figure 2 of *Yue et al.* [2013]). Thus earthward electric field drift will be larger, and particles will experience a larger Bz change, along $Y = 0$ than away from midnight. This should result in larger adiabatic energization and pressure increase at midnight. The effect of the previous substorm represented by *AE* loading is also not uniform across the tail. As shown in *Wing et al.* [2007], the pressure increase after a substorm onset is larger near midnight than away from midnight, thus contributing to higher pressure near midnight for the growth phase of the following substorm.

As shown in the right column, the model pressure under a fixed energy loading increases nonlinearly as sunspot number increases. The model pressure at smaller r increases first then decreases, showing a peak value around sunspot number of ~80, which is consistent with the observations shown in Figure 2c. The pressure shows little change under smaller sunspot number farther from the Earth, while it decreases then increases at higher sunspot number, showing a dip around sunspot number of ~110. The sunspot number has been shown to correlate with different solar wind structures and polar cap conductance [*Gonzalez et al.*, 1999; *Ohtani et al.*, 2014]. Previous studies [e.g., *Borovsky and Denton*, 2006] also showed that the high-speed solar wind is more likely generated at the declining phase of a solar cycle when the sunspot number has decreased to near half of the peak value at solar maximum. This correlation is seen in our data set. For a given P_{SW} and energy loading, the solar wind velocity maximizes at sunspot number of ~60–80 while the solar wind number density reaches the lowest. Since there are strong and positive correlations between solar wind velocity and the plasma sheet temperature and between the solar wind number density and plasma sheet density [*Borovsky et al.*, 1997], one would expect statistically that the plasma sheet is hotter and more tenuous

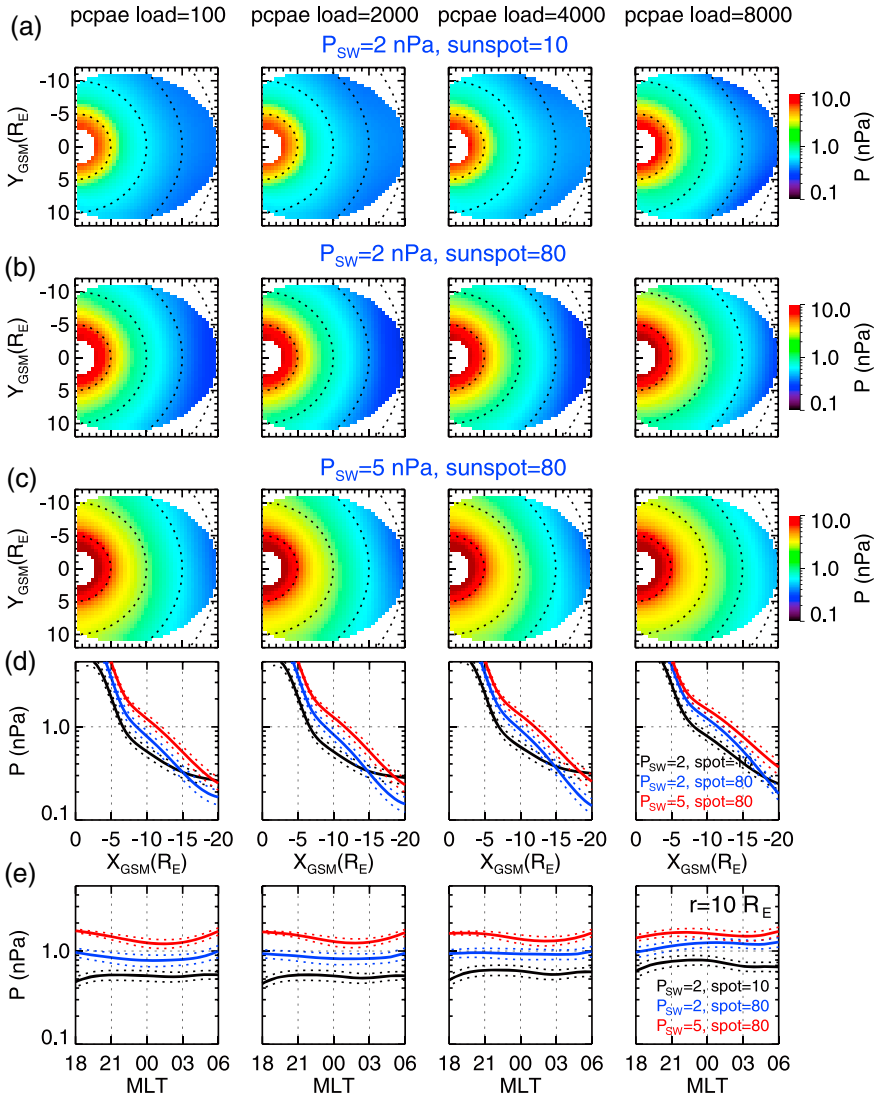

Figure 10. Distribution of modeled pressures on the equatorial plane and their radial and azimuthal (at $r = 10\ R_E$) profiles with error bounds for four energy loading cases (PCPAE loading = 100, 2000, 4000, and 8000 kV min) with different control parameters: (a) $P_{SW} = 2$ nPa, sunspot = 10; (b) $P_{SW} = 2$ nPa, sunspot = 80; and (c) $P_{SW} = 5$ nPa, sunspot = 80. (d and e) The radial and azimuthal pressure profile with different control parameters. The black, blue, and red lines are for $P_{SW} = 2$ nPa, sunspot = 10; $P_{SW} = 2$ nPa, sunspot = 80; and $P_{SW} = 5$ nPa, sunspot = 80, respectively.

when the sunspot number is near 60–80. Also, it has been shown that the plasma sheet pressure is generally higher for hot-tenuous plasma sheet than cold-dense plasma sheet [*Wang et al.,* 2009, 2010]; the plasma sheet pressure is likely to be the highest when the sunspot number is ~60–80. In addition, simulations from *Gkioulidou et al.* [2009] have shown that under the same CPCP driving, the shielding of convection electric field is less effective when the plasma sheet is hotter and more tenuous. As a result, plasma sheet pressure in the inner edge of the plasma sheet is farther earthward and the plasma sheet pressure is higher for a hotter and more tenuous plasma sheet [see *Gkioulidou et al.*, 2009, Figure 5]. These previous studies thus provide a reasonable explanation for the dependence on the sunspot number and the larger dependences seen at smaller $|X|$.

Figures 10a–10c show the equatorial pressure distributions for four different loadings (100, 2000, 4000, and 8000 kV min) when $P_{SW} = 2$ or 5 nPa and sunspot number = 10 or 80 (80 is approximately the median sunspot number as shown in Figure 5a). As shown in Figure 4, these four loading values are typically seen at different

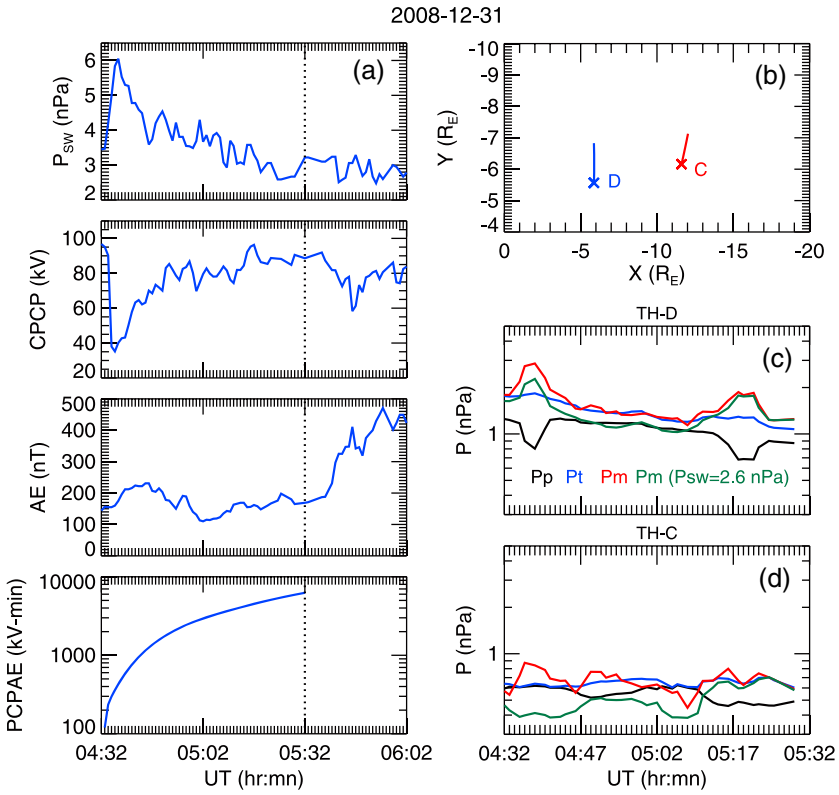

Figure 11. Example of modeled and observed pressure comparison during 60 min growth phase of 31 December 2008 substorm. The substorm onset occurred at 05:32 UT identified from auroral images. (a) The variation of P_{SW}, CPCP, *AE*, and PCPAE loading based on OMNI data 1 h prior to and 30 min after onset. The dashed vertical line marks the substorm onset time. (b) TH-C and TH-D trajectories at *X-Y* plane in GSM coordinates. The blue and red lines are the TH-D and TH-C, respectively. (c and d) The comparison of the modeled and observed pressures from TH-D and TH-C. The black, blue, green, and red lines are the observed plasma pressure, total pressures, the model pressure with constant $P_{SW} = 2.6$ nPa, and the modeled pressure with time-dependent P_{SW}, respectively.

growth phase stages of a moderate substorm with 100 at the beginning, 2000 and 4000 at the middle, and 8000 at the end of the growth phase. Their midnight profiles are shown in Figure 10d. The overall predicted pressures are higher when under higher energy loading or P_{SW}. On the other hand, under the same loading and P_{SW}, pressures at median sunspot number are found to be higher in the near-Earth region but lower in the tail compared to those at low sunspot number (also compared to those at high sunspot number, not shown). Figure 10e shows the azimuthal profiles at $r = 10\,R_E$. The pressures are more dawn-dusk asymmetric with higher pressure in the premidnight Magnetic Local Time (MLTs) when P_{SW} is higher or the sunspot number is closer to the median values. These asymmetries become weaker when loading is higher.

4.2. A Substorm Event Study

The spatial structure of the growth phase pressure and its quantitative correlations with different factors predicted by our empirical model can be used to understand the pressure changes observed by spacecraft during substorm events. Here we show an example of a substorm on 31 December 2008 (the onset occurred at ~05:38 UT from the *AL* drop but at ~05:32 from aurora). This event is chosen for having a large and monotonic change in P_{SW}. Figure 11a shows the variations of P_{SW}, CPCP, *AE*, and PCPAE loading. During the growth phase, P_{SW} increased from 3.5 to 6 nPa in the first 5 min, then decreased gradually from ~6 to 2.6 nPa with some small fluctuations. Meanwhile, CPCP decreased sharply in the first 3 min, then gradually increased from ~35 to 90 kV and remained around 90 kV after ~05:15 UT. *AE* was high at the beginning because of the previous substorm. It decreased to 100 nT in about 20 min and then increased back to 200 nT prior to the onset (the vertical dashed line in Figure 11a marks the onset time), and *AE* max after the onset is ~480 nT.

ThePCPAE loading increased from ~100 to 6000 kV min, corresponding to a typical moderate substorm as shown in Figure 4.

Figure 11b shows the trajectories of TH-C and TH-D in the *X-Y* plane in GSM coordinates during the growth phase. TH-D was at $r \sim 6\ R_E$ while TH-C was at $r \sim 12\ R_E$ and both were moving eastward and farther away from midnight. As shown in Figures 11c and 11d, they remained near the plasma sheet for most of the growth phase as indicated by the comparable magnitudes between the plasma pressures (black line) and total pressures (blue line), except for TH-D for two very brief durations at the beginning and near the end of the growth phase. We then predicted the evolution of pressures with the temporal profiles of the control parameters (X_{GSM}, Y_{GSM}, *Br*, P_{SW}, PCPAE loading, and the monthly averaged sunspot number = 0.8). To illuminate the effect of P_{SW} changes, we also evaluated the pressure change using constant $P_{SW} = 2.6$ nPa (the lowest P_{SW} during the growth phase). The model results and corresponding observations from TH-D and TH-C during the substorm growth phase are shown in Figures 11c and 11d, respectively. The predicted total pressures with time-dependent P_{SW} and constant P_{SW} are indicated by the red and green lines, respectively. It can be seen that the total pressure (blue line) observed by TH-D gradually decreased from ~1.8 to 1 nPa during the substorm growth phase. The predicted pressure with time-dependent P_{SW} (red line) agrees well in general with the observed pressure (blue line) in both magnitudes and its decreasing trend, except the two very short periods when TH-D went suddenly farther away from the current sheet at ~4:35 and ~05:20 UT. *Br* during these two periods was >40 nT and exceeded the reliable *Br* range (<30 nT) for the pressure model, thus causing the discrepancy between the predicted and observed pressures. In comparison, the predicted pressure at TH-D with constant P_{SW} (green line) still shows a slight decreasing trend despite that globally the plasma pressure is increasing under increasing loading. This is because TH-D was moving farther away from midnight to a location where, as shown in Figure 9, the pressure is relatively lower and the pressure increase in response to increasing loading is also smaller. The local temporal pressure increase is smaller than the spatial pressure decrease along TH-D trajectory, resulting in the slight pressure decrease under constant P_{SW}. Thus, the observed substantial pressure decrease at TH-D should be mainly due to the decreasing P_{SW}.

On the other hand, at TH-C, both the observed pressure (blue line) and the predicted pressure with time-dependent P_{SW} (red line) show little change as the growth phase proceeds, and the two pressures are in good agreement. The predicted pressure with constant P_{SW} (green line) increases with time, contrary to the prediction at TH-D. This is because the loading effect is stronger at larger *r*, so the local temporal pressure increase exceeds the spatial decrease along the TH-C trajectory. However, this pressure increase due to the energy loading alone is similar to the decrease in response to the decreasing P_{SW} alone, resulting in no substantial pressure changes observed by TH-C. This event study shows that, despite under increasing energy loading, it is not necessary for spacecraft to see a pressure increase during the substorm growth phase, which in fact is quite common, because of the P_{SW} effect as well as the combined temporal and spatial effect along spacecraft trajectory as discussed above.

5. Summary and Conclusion

In order to understand changes in the pressure spatial distribution in the inner plasma sheet ($r \leq 20\ R_E$) during the substorm growth phase, we have identified the factors that are well correlated with plasma sheet pressure and its corresponding changes and built up a 2-D equatorial empirical plasma sheet pressure model and an error model by using the Support Vector Regression Machine (SVRM) controlled by these factors. Major results from this study are the following:

1. Based on our large database of ~2,800,000 plasma pressure data points during substorm growth phase from THEMIS and Geotail observations from year 1995 to 2010, we identified P_{SW}, energy loading, and the sunspot number as the three primary contributors to pressure variations. Here the energy loading is a combination of time integral of CPCP and *AE* that we found is a better representative of energy loading.
2. By using these factors as inputs and using the Support Vector Regression Machine technique, we have successfully constructed a 2-D plasma sheet pressure model that has high accuracy with 5% median errors. Data and model comparison indicates that the new pressure model represents observations very well in general. The predicted pressure gradients also agree reasonably well with the observed pressure gradients obtained from simultaneous THEMIS two-probe measurements.

3. We have found that the pressure increases linearly as P_{SW} increases. The pressure increase ratios are larger under lower energy loading but similar at different regions. On the other hand, the pressure responses to energy loading and sunspot number are nonlinear. The pressure increases first with increasing loading or sunspot number; it then remains relatively constant or decreases slightly after reaching a peak value at loading of ~8000 kV min or at sunspot number of ~80. The loading effect is stronger when P_{SW} is lower. It is similar at different radial distance but stronger near midnight than away from midnight. The effect of sunspot number is more clearly seen at smaller r.
4. Our pressure model can be used to understand the pressure changes observed during a substorm event by providing evaluations of the individual and combined effects of energy loading and P_{SW}, as well as the combined temporal and spatial effect along the spacecraft trajectory.

In future studies, we will use the 2-D pressure distributions predicted by this empirical pressure model as inputs to obtain 3-D force-balanced magnetic field configurations using our force-balanced magnetic field modeling [*Yue et al.,* 2013, 2014]. This will allow us to investigate the pressure and magnetic field configuration changes as pre-onset conditions and evaluate whether the changes can lead to unstable plasma sheet, such as the interchange or ballooning instability.

Acknowledgments

The work by C. Yue, C.-P. Wang, and L.R. Lyons at UCLA has been supported by NASA grants NNX11AJ12G and NNX08A135G, NSF grant ATM-1003595, and IGPPS Program at Los Alamos National Laboratory. We also acknowledge Jianzhu Ma (Toyota Technological Institute at Chicago, Chicago, USA) for the very helpful discussion of SVRM. And the LibSVM can be found online at http://www.csie.ntu.edu.tw/~cjlin/libsvm/. All Geotail data are from the Institute of Space and Astronautical Science/Japan Aerospace Exploration Agency (ISAS/JAXA) through the Data Archives and Transmission System (DARTS) of ISAS (http://www.darts.isas.jaxa.jp/). All THEMIS data are from THEMIS official website (http://themis.ssl.berkeley.edu/data_files.shtml). And the solar wind, IMF parameters, and the geomagnetic indices were obtained from the NASA OMNI database. The observed monthly sunspot numbers are from the "radio and space weather service" website (http://www.ips.gov.au/Solar/1/6).

Larry Kepko thanks the reviewers for their assistance in evaluating this paper.

References

Angelopoulos, V. (1996), The role of impulsive particle acceleration in magnetotail circulation, in *Proceedings of the Third International Conference on Substorms (ICS-3)*, *Spec. Publ.*, vol. 389, pp. 17–22, Eur. Space Agency, Noordwijk, Netherlands.

Angelopoulos, V., et al. (1993), Characteristics of ion flow in the quiet state of the inner plasma sheet, *Geophys. Res. Lett.*, *20*, 1711–1714, doi:10.1029/93GL00847.

Auster, H. U., et al. (2008), The THEMIS fluxgate magnetometer, *Space Sci. Rev.*, *141*, 235–264, doi:10.1007/s11214-008-9365-9.

Baker, D. N., and R. L. McPherron (1990), Extreme energetic particle decreases near geostationary orbit: A manifestation of current diversion within the inner plasma sheet, *J. Geophys. Res.*, *95*(A5), 6591–6599, doi:10.1029/JA095iA05p06591.

Ban, P.-P., S.-J. Sun, C. Chen, and Z.-W. Zhao (2011), Forecasting of low-latitude storm-time ionospheric f_oF_2 using support vector machine, *Radio Sci.*, *46*, RS6008, doi:10.1029/2010RS004633.

Baumjohann, W., G. Paschmann, and H. Lühr (1990), Pressure balance between lobe and plasma sheet, *Geophys. Res. Lett.*, *17*, 45–48, doi:10.1029/GL017i001p00045.

Borovsky, J. E., and M. H. Denton (2006), Differences between CME-driven storms and CIR-driven storms, *J. Geophys. Res.*, *111*, A07S08, doi:10.1029/2005JA011447.

Borovsky, J. E., M. F. Thomsen, and D. J. McComas (1997), The superdense plasma sheet: Plasmaspheric origin, solar wind origin, or ionospheric origin?, *J. Geophys. Res.*, *102*(A10), 22,089–22,097, doi:10.1029/96JA02469.

Borovsky, J. E., M. F. Thomsen, and R. C. Elphic (1998), The driving of the plasma sheet by the solar wind, *J. Geophys. Res.*, *103*(A8), 17,617–17,640, doi:10.1029/97JA02986.

Chang, C. C., and C. J. Lin (2001), LIBSVM: A library for support vector machines, Tech. Rep., National Taiwan Univ. [Available at http://www.csie.ntu.edu.tw/cjlin/libsvm.]

Drucker, H., C. J. C. Burges, L. Kaufman, A. Smola, and V. Vapnik (1997), *Support Vector Regression Machines,* Vol. 9, *Advances in Neural Information Processing Systems, NIPS 1996*, pp. 155–161, MIT Press, Denver, Colo.

Fairfield, D. H., R. P. Lepping, E. W. Hones Jr., S. J. Bame, and J. R. Asbridge (1981), Simultaneous measurements of magnetotail dynamics by IMP spacecraft, *J. Geophys. Res.*, *86*, 1396–1414, doi:10.1029/JA086iA03p01396.

Gavrishchaka, V. V., and S. B. Ganguli (2001), Support vector machine as an efficient tool for high-dimensional data processing: Application to substorm forecasting, *J. Geophys. Res.*, *106*(A12), 29,911–29,914, doi:10.1029/2001JA900118.

Gkioulidou, M., C.-P. Wang, L. R. Lyons, and R. A. Wolf (2009), Formation of the Harang reversal and its dependence on plasma sheet conditions: Rice convection model simulations, *J. Geophys. Res.*, *114*, A07204, doi:10.1029/2008JA013955.

Gonzalez, W. D., B. T. Tsurutani, and A. L. Clua de Gonzales (1999), Interplanetary origin of geomagnetic storms, *Space Sci. Rev.*, *88*, 529.

Hsu, T.-S., and R. L. McPherron (2012), A statistical analysis of substorm associated tail activity, *Adv. Space Res.*, *50*(10), 1317–1343, doi:10.1016/j.asr.2012.06.034.

Huang, C., D.-D. Liu, and J.-S. Wang (2009), Forecast daily indices of solar activity, F10.7, using support vector regression method, *Res. Astron. Astrophys.*, *9*, 694.

Kokubun, S., T. Yamamoto, M. H. Acuna, K. Hayashi, K. Shiokawa, and H. Kawano (1994), The Geotail magnetic field experiment, *J. Geomagn. Geoelectr.*, *46*, 7–21, doi:10.5636/jgg.46.7.

Liu, D. D., C. Huang, J. Y. Lu, and J. S. Wang (2011), The hourly average solar wind velocity prediction based on support vector regression method, *Mon. Not. R. Astron. Soc.*, *413*, 2877–2882, doi:10.1111/j.1365-2966.2011.18359.x.

Liu, W. W. (1997), Physics of the explosive growth phase: Ballooning instability revisited, *J. Geophys. Res.*, *102*(A3), 4927–4931, doi:10.1029/96JA03561.

Machida, S., Y. Miyashita, A. Ieda, M. Nosé, D. Nagata, K. Liou, T. Obara, A. Nishida, Y. Saito, and T. Mukai (2009), Statistical visualization of the Earth's magnetotail based on Geotail data and the implied substorm model, *Ann. Geophys.*, *27*, 1035–1046.

McFadden, J. P., C. W. Carlson, D. Larson, V. Angelopoulos, M. Ludlam, R. Abiad, B. Elliott, P. Turin, and M. Marckwordt (2008), The THEMIS ESA plasma instrument and in-flight calibration, *Space Sci. Rev.*, *141*, 277–302, doi:10.1007/s11214-008-9440-2.

McPherron, R. L. (1970), Growth phase of magnetospheric substorms, *J. Geophys. Res.*, *75*(28), 5592–5599, doi:10.1029/JA075i028p05592.

Miura, A., S. Ohtani, and T. Tamao (1989), Ballooning instability and structure of diamagnetic hydromagnetic waves in a model magnetosphere, *J. Geophys. Res.*, *94*(A11), 15,231–15,242, doi:10.1029/JA094iA11p15231.

Miyashita, Y., S. Machida, T. Mukai, Y. Saito, K. Tsuruda, H. Hayakawa, and P. R. Sutcliffe (2000), A statistical study of variations in the near and middistant magnetotail associated with substorm onsets: Geotail observations, *J. Geophys. Res.*, *105*(A7), 15,913–15,930, doi:10.1029/1999JA000392.

Miyashita, Y., S. Machida, T. Mukai, Y. Saito, and P. R. Sutcliffe (2001), Mass and energy transport in the near and middistant magnetotail around substorm onsets: Geotail observations, *J. Geophys. Res.*, *106*(A4), 6259–6274, doi:10.1029/2000JA000233.

Miyashita, Y., S. Machida, K. Liou, T. Mukai, Y. Saito, H. Hayakawa, C.-I. Meng, and G. K. Parks (2003), Evolution of the magnetotail associated with substorm auroral breakups, *J. Geophys. Res.*, *108*(A9), 1353, doi:10.1029/2003JA009939.

Miyashita, Y., et al. (2009), A state-of-the-art picture of substorm-associated evolution of the near-Earth magnetotail obtained from superposed epoch analysis, *J. Geophys. Res.*, *114*, A01211, doi:10.1029/2008JA013225.

Miyashita, Y., et al. (2010), Pressure changes associated with substorm depolarization in the near-Earth plasma sheet, *J. Geophys. Res.*, *115*, A12239, doi:10.1029/2010JA015608.

Mukai, T., S. Machida, Y. Saito, M. Hirahara, T. Terasawa, N. Kaya, T. Obara, M. Ejiri, and A. Nishida (1994), The low energy particle (LEP) experiment onboard the Geotail satellite, *J. Geomagn. Geoelectr.*, *46*, 669–692, doi:10.5636/jgg.46.669.

Nishimura, Y., L. R. Lyons, V. Angelopoulos, T. Kikuchi, S. Zou, and S. B. Mende (2011), Relations between multiple auroral streamers, pre-onset thin arc formation, and substorm auroral onset, *J. Geophys. Res.*, *116*, A09214, doi:10.1029/2011JA016768.

Noble, W. S. (2006), What is a support vector machine?, *Nat. Biotechnol.*, *24*, 1565–1567.

Ohtani, S., S. Wing, V. G. Merkin, and T. Higuchi (2014), Solar cycle dependence of nightside field-aligned currents: Effects of dayside ionospheric conductivity on the solar wind-magnetosphere-ionosphere coupling, *J. Geophys. Res. Space Physics*, *119*, 322–334, doi:10.1002/2013JA019410.

Petrinec, S. M., and C. T. Russell (1993), An empirical model of the size and shape of the near-Earth magnetotail, *Geophys. Res. Lett.*, *20*(23), 2695–2698, doi:10.1029/93GL02847.

Pu, Z. Y., A. Korth, Z. X. Chen, R. H. W. Friedel, Q. G. Zong, X. M. Wang, M. H. Hong, S. Y. Fu, Z. X. Liu, and T. I. Pulkkinen (1997), MHD drift ballooning instability near the inner edge of the near-Earth plasma sheet and its application to substorm onset, *J. Geophys. Res.*, *102*(A7), 14,397–14,406, doi:10.1029/97JA00772.

Sanny, J., R. L. McPherron, C. T. Russell, D. N. Baker, T. I. Pulkkinen, and A. Nishida (1994), Growth-phase thinning of the near-Earth current sheet during the CDAW 6 substorm, *J. Geophys. Res.*, *99*, 5805–5816, doi:10.1029/93JA03235.

Sergeev, V., V. Angelopoulos, M. Kubyshkina, E. Donovan, X. Z. Zhou, A. Runov, H. Singer, J. McFadden, and R. Nakamura (2011), Substorm growth and expansion onset as observed with ideal ground-spacecraft THEMIS coverage, *J. Geophys. Res.*, *116*, A00I26, doi:10.1029/2010JA015689.

Sergeev, V. A., P. Tanskanen, K. Mursula, A. Korth, and R. C. Elphic (1990), Current sheet thickness in the near-Earth plasma sheet during substorm growth phase, *J. Geophys. Res.*, *95*, 3819–3828, doi:10.1029/JA095iA04p03819.

Shue, J.-H., J. K. Chao, H. C. Fu, C. T. Russell, P. Song, K. K. Khurana, and H. J. Singer (1997), A new functional form to study the solar wind control of the magnetopause size and shape, *J. Geophys. Res.*, *102*(A5), 9497–9511, doi:10.1029/97JA00196.

Spence, H. E., and M. G. Kivelson (1993), Contributions of the low-latitude boundary layer to the finite width magnetotail convection model, *J. Geophys. Res.*, *98*, 15,487–15,496, doi:10.1029/93JA01531.

Spence, H. E., M. G. Kivelson, R. J. Walker, and D. J. McComas (1989), Magnetospheric plasma pressures in the midnight meridian: Observations from 2.5 to 35 R_E, *J. Geophys. Res.*, *94*(A5), 5264–5272, doi:10.1029/JA094iA05p05264.

Tsyganenko, N. A., and T. Mukai (2003), Tail plasma sheet models derived from Geotail particle data, *J. Geophys. Res.*, *108*(A3), 1136, doi:10.1029/2002JA009707.

Vapnik, V., and A. Lerner (1963), Pattern recognition using generalized portrait method, *Autom. Rem. Contr.*, *24*, 774–780.

Wang, C. P., L. R. Lyons, J. M. Weygand, T. Nagai, and R. W. McEntire (2006), Equatorial distributions of the plasma sheet ions, their electric and magnetic drifts, and magnetic fields under different interplanetary magnetic field Bz conditions, *J. Geophys. Res.*, *111*, A04215, doi:10.1029/2005JA011545.

Wang, C. P., L. R. Lyons, R. A. Wolf, T. Nagai, J. M. Weygand, and A. T. Y. Lui (2009), Plasma sheet $PV^{5/3}$ and nV and associated plasma and energy transport for different convection strengths and *AE* levels, *J. Geophys. Res.*, *114*, A00D02, doi:10.1029/2008JA013849.

Wang, C.-P., L. R. Lyons, T. Nagai, J. M. Weygand, and A. T. Y. Lui (2010), Evolution of plasma sheet particle content under different interplanetary magnetic field conditions, *J. Geophys. Res.*, *115*, A06210, doi:10.1029/2009JA015028.

Wang, C.-P., Y. Chao, S. Zaharia, X. Xing, L. Lyons, V. Angelopoulos, T. Nagai, and T. Lui (2013), Empirical modeling of plasma sheet pressure and three-dimensional force-balanced magnetospheric magnetic field structure: 1. Observation, *J. Geophys. Res. Space Physics*, *118*, 6154–6165, doi:10.1002/jgra.50585.

Wang, Y., D. G. Sibeck, J. Merka, S. A. Boardsen, H. Karimabadi, T. B. Sipes, J. Šafránková, K. Jelínek, and R. Lin (2013), A new three-dimensional magnetopause model with a support vector regression machine and a large database of multiple spacecraft observations, *J. Geophys. Res. Space Physics*, *118*, 2173–2184, doi:10.1002/jgra.50226.

Weimer, D. R. (1995), Models of high-latitude electric potentials derived with a least error fit of spherical harmonic coefficients, *J. Geophys. Res.*, *100*, 19,595–19,608, doi:10.1029/95JA01755.

Williams, D. J., R. W. McEntire, C. Schlemm II, A. T. Y. Lui, G. Gloeckler, S. P. Christon, and F. Gliem (1994), Geotail energetic particles and ion composition instrument, *J. Geomagn. Geoelectr.*, *46*, 39–57, doi:10.5636/jgg.46.39.

Wing, S., J. W. Gjerloev, J. R. Johnson, and R. A. Hoffman (2007), Substorm plasma sheet ion pressure profiles, *Geophys. Res. Lett.*, *34*, L16110, doi:10.1029/2007GL030453.

Xing, X., L. R. Lyons, V. Angelopoulos, D. Larson, C. Carlson, A. Runov, and U. Auster (2010), Plasma sheet pressure evolution related to substorms, *J. Geophys. Res.*, *115*, A01212, doi:10.1029/2009JA014315.

Xing, X., L. R. Lyons, Y. Nishimura, V. Angelopoulos, E. Donovan, E. Spanswick, J. Liang, D. Larson, C. Carlson, and U. Auster (2011), Near-Earth plasma sheet azimuthal pressure gradient and associated auroral development soon before substorm onset, *J. Geophys. Res.*, *116*, A07204, doi:10.1029/2011JA016539.

Yue, C., C.-P. Wang, S. G. Zaharia, X. Xing, and L. Lyons (2013), Empirical modeling of plasma sheet pressure and three-dimensional force-balanced magnetospheric magnetic field structure: 2. Modeling, *J. Geophys. Res. Space Physics*, *118*, 6166–6175, doi:10.1002/2013JA018943.

Yue, C., C.-P. Wang, L. Lyons, J. Liang, E. F. Donovan, S. G. Zaharia, and M. Henderson (2014), Current sheet scattering and ion isotropic boundary under 3D empirical force-balanced magnetic field, *J. Geophys. Res. Space Physics*, *119*, 8202–8211, doi:10.1002/2014JA020172.